Deviation from Fermi-liquid transport behavior in the vicinity of a Van Hove singularity

Herman, František ; Buhmann, Jonathan ; Fischer, Mark H ; Sigrist, Manfred

Abstract: Recent experiments revealed non-Fermi-liquid resistivity in the unconventional superconductor Sr_2RuO_4 when strain pushes one of the Fermi surfaces close to a van Hove singularity. The origin of this behavior and whether it can be understood from a picture of well-defined quasiparticles is unclear. We employ a Boltzmann transport analysis beyond the single relaxation-time approximation based on a single band which undergoes a Lifshitz transition where the Fermi surface crosses a van Hove singularity either due to uniaxial or epitaxial strain. First, analytically investigating impurity scattering, we clarify the role of the diverging density of states together with the locally flat band at the point of the Lifshitz transition. Additionally, including electron-electron scattering numerically, we find good qualitative agreement with resistivity measurements on uniaxially strained Sr_2RuO_4, including the temperature scaling and the temperature dependence of the resistivity peak. Our results imply that, even close to the Lifshitz transition, a description starting from well-defined quasiparticles holds. To test the validity of Boltzmann transport theory near a van Hove singularity, we provide further experimentally accessible parameters, such as thermal transport, the Seebeck coefficient, and Hall resistivity and compare different strain scenarios.

DOI: https://doi.org/10.1103/physrevb.99.184107

Deviation from Fermi-liquid transport behavior in the vicinity of a Van Hove singularity

František Herman,[1] Jonathan Buhmann,[1] Mark H. Fischer,[2,1] and Manfred Sigrist[1]
[1]*Institute for Theoretical Physics, ETH Zurich, 8093 Zurich, Switzerland*
[2]*Department of Physics, University of Zurich, 8057 Zurich, Switzerland*

(Received 8 March 2019; published 17 May 2019)

Recent experiments revealed non-Fermi-liquid resistivity in the unconventional superconductor Sr_2RuO_4 when strain pushes one of the Fermi surfaces close to a van Hove singularity. The origin of this behavior and whether it can be understood from a picture of well-defined quasiparticles is unclear. We employ a Boltzmann transport analysis beyond the single relaxation-time approximation based on a single band which undergoes a Lifshitz transition where the Fermi surface crosses a van Hove singularity either due to uniaxial or epitaxial strain. First, analytically investigating impurity scattering, we clarify the role of the diverging density of states together with the locally flat band at the point of the Lifshitz transition. Additionally, including electron-electron scattering numerically, we find good qualitative agreement with resistivity measurements on uniaxially strained Sr_2RuO_4, including the temperature scaling and the temperature dependence of the resistivity peak. Our results imply that, even close to the Lifshitz transition, a description starting from well-defined quasiparticles holds. To test the validity of Boltzmann transport theory near a van Hove singularity, we provide further experimentally accessible parameters, such as thermal transport, the Seebeck coefficient, and Hall resistivity and compare different strain scenarios.

DOI: 10.1103/PhysRevB.99.184107

I. INTRODUCTION

Fermi-liquid theory, which establishes a one-to-one mapping of electrons to well-defined quasiparticles, is the basis of our understanding of metals. Its validity as well as its breakdown are often characterized through transport properties. In particular, the quadratic temperature dependence of the resistivity $\rho = \rho_0 + AT^2$ due to electron-electron scattering and the linear-in-T Seebeck coefficient Q are hallmarks of a Fermi liquid. Despite the theory's great success in describing most metals, some classes of systems are known to violate these expectations, most notably interacting fermions in one dimension and systems close to a quantum critical point.

Bringing the Fermi surface close to a van Hove singularity (vHS) in two dimensions, i.e., a point of diverging density of states, provides another example, where non-Fermi-liquid behavior can be observed. Whether such behavior is associated with a breakdown in Fermi-liquid theory and the disappearance of well-defined quasiparticles is, however, not well established. Indeed, Buhmann [1] showed how nongeneric transport behavior can be observed within a picture of well-defined quasiparticles subject to electron-electron (umklapp) scattering close to a vHS.

Experimentally, modifying the Fermi energy through doping and thus moving the Fermi surface close to a vHS, on one hand, is straightforward. However, this introduces disorder into the system, making comprehensive transport studies impossible. Fermi-surface engineering through tensile or compressive strain, on the other hand, provides a noninvasive method for tuning the electronic structure of a material [2–5]. Indeed, recent experiments have demonstrated both routes on the single-layer perovskite Sr_2RuO_4, which, at low temperatures, exhibits almost perfect Fermi-liquid behavior below $T \approx 50$ K [6] before entering a superconducting state at $T_c \approx 1.5$ K. Interestingly, the so-called γ band, stemming mostly from Ru d_{xy} orbitals, nearly touches the Brillouin zone (BZ) boundary where the vHS is located [7] and is, therefore, most interesting in connection with Fermi-surface tuning.

Barber *et al.* [8] showed that uniaxial stress can be used as a tuning knob for the normal state resistivity. Here, density functional theory (DFT) calculations indicate that the γ Fermi surface undergoes a Lifshitz transition [9] [see Fig. 1(b)] at a critical stress that in resistivity measurements coincides with a pronounced peak at low temperatures and T-linear scaling above. An alternative route for Fermi-surface engineering was demonstrated by Burganov *et al.* [10], who epitaxially grew thin films on lattice-mismatched substrates. The resulting strain leads to a redistribution of electrons within the t_{2g} manifold effectively doping the γ band. This effective doping can induce a Lifshitz transition as well with associated crossing of a vHS as indicated in Fig. 1(a), and deviations from T^2 behavior were observed in the resistivity on the samples close to the transition. Having access to the exposed surface, this setup additionally allows for characterization of the electronic structure using scanning tunneling microscopy and angle-resolved photoemission spectroscopy.

Previous work on the effect of a Lifshitz transition on transport properties used approximations to the electron-electron scattering within a Green's function method or through weighted scattering probabilities [11–15]. Our approach is based on analyses (both analytic and numerical) of the general transport coefficients within a Boltzmann-equation approach including effects of umklapp scattering. The aim of our paper is then twofold: First, our numerical approach goes beyond the standard relaxation-time approximation as we use the full angular momentum dependence of the scattering. Taking

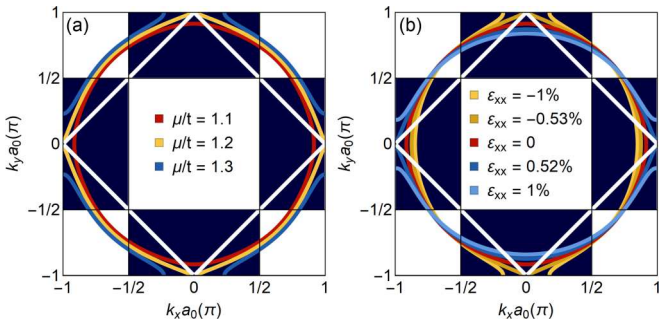

FIG. 1. Fermi surface tuned through the vHS at $(\pi, 0)$ or $(0, \pi)$ by (a) adjusting the chemical potential (doping) and (b) applying uniaxial stress. The dark areas (white diamond) denote regions where umklapp scattering by $(2\pi, 0)$ or $(0, 2\pi)$ [$(2\pi, 2\pi)$] is possible.

both impurity scattering and interaction effects, including umklapp scattering into account, allows for a careful comparison to existing experimental results of electrical transport upon Fermi-surface tuning. The observed agreement with experiment establishes that well-defined quasiparticles are indeed capable of capturing all observed trends. Second, we predict further transport signatures near the vHS, such as thermal transport, the Seebeck coefficient, the Hall effect, a violation of the Wiedemann-Franz law, and the Kadowaki-Woods ratio. Here, we compare the two scenarios of crossing the vHS at all four boundaries of the Brillouin zone and the Lifshitz transition only at two points in the direction parallel or orthogonal to an applied electrical field, see Figs. 1(a) and 1(b). These predictions allow for additional comparison of the vHS scenario within a picture of well-defined quasiparticles to experiment.

In the following, we first introduce the general Boltzmann formalism and model-specific details for both types of scatterings. An analytical discussion of electrical transport for impurity scattering which is mainly relevant for the low-temperature regime explains some of the main features connected with the crossing of the Fermi surface through the vHS. Then, we will turn to the numerical discussion and examine the different transport properties showing how deviations from standard Fermi-liquid behavior occur in connection with the Lifshitz transitions within both scenarios of Fermi-surface tuning. As we can reproduce many of the experimental findings within our calculation, we conclude that the non-Fermi-liquid behavior can be accounted for within the picture of intact quasiparticles. Many of the calculated quantities have not been investigated on real systems so far such that our results could be further tested in experiment.

II. BOLTZMANN APPROACH

We investigate general transport properties by solving the Boltzmann transport equation,

$$(\partial_t + \dot{\boldsymbol{r}} \cdot \nabla_{\boldsymbol{r}} + \dot{\boldsymbol{p}} \cdot \nabla_{\boldsymbol{p}}) f(\boldsymbol{u}) = [\partial_t f(\boldsymbol{u})]_{\text{imp}} + [\partial_t f(\boldsymbol{u})]_{\text{el-el}}, \tag{1}$$

where $\boldsymbol{u} = \{t, \boldsymbol{r}, \boldsymbol{p}\}$ denotes extended phase-space coordinates and $f(\boldsymbol{u})$ is the (spin-independent) distribution function. In the following, we are interested in the homogeneous stationary solution such that $f(\boldsymbol{u}) \equiv f(\boldsymbol{p})$. The left-hand side of Eq. (1) includes the effect of temperature gradients and fields through the substantial time derivative. The right-hand side includes, in our case, the input from impurity and electron-electron scattering. Assuming Matthiesen's rule to apply, we can treat the two contributions separately. Impurity scattering is formulated as

$$[\partial_t f(\boldsymbol{p})]_{\text{imp}} = -\Omega \int (d\boldsymbol{p}') \Gamma^{\text{imp}}_{\boldsymbol{p},\boldsymbol{p}'} \{ f(\boldsymbol{p})[1 - f(\boldsymbol{p}')] - [1 - f(\boldsymbol{p})] f(\boldsymbol{p}') \}, \tag{2}$$

where $(d\boldsymbol{p}) = d\boldsymbol{p}/(2\pi\hbar)^2$, Ω is the sample volume and scattering rates are determined by the Fermi golden rule,

$$\Gamma^{\text{imp}}_{\boldsymbol{p},\boldsymbol{p}'} = \frac{2\pi}{\hbar} n_{\text{imp}} |v_{\text{imp}}|^2 \delta(\varepsilon_{\boldsymbol{p}} - \varepsilon_{\boldsymbol{p}'}). \tag{3}$$

Here, n_{imp} is the density of impurities, and $v_{\text{imp}} = \langle \boldsymbol{p} | \hat{V}_{\text{imp}} | \boldsymbol{p}' \rangle$ is the scattering matrix element, which we assume to be isotropic, considering only s-wave (contact) scattering. We introduce the dimensionless impurity scattering strength $n_{\text{imp}}|v_{\text{imp}}|^2/t^2 = 0.01$, where t is the characteristic energy scale of the electron dispersion $\varepsilon_{\boldsymbol{p}}$ as described in Appendix A.

The effect of a collision between electrons is included in the second term on the right-hand side of Eq. (1),

$$[\partial_t f(\boldsymbol{p}_1)]_{\text{el-el}} = -\Omega^3 \int (d\boldsymbol{p}_2)(d\boldsymbol{p}_3)(d\boldsymbol{p}_4) \Gamma^{\text{el-el}}_{\boldsymbol{p}_1 - \boldsymbol{p}_4} \times \{ f(\boldsymbol{p}_1) f(\boldsymbol{p}_2)[1 - f(\boldsymbol{p}_3)][1 - f(\boldsymbol{p}_4)] - [1 - f(\boldsymbol{p}_1)][1 - f(\boldsymbol{p}_2)] f(\boldsymbol{p}_3) f(\boldsymbol{p}_4) \}, \tag{4}$$

whereby the two electrons change their momenta $(\boldsymbol{p}_1, \boldsymbol{p}_2) \leftrightarrow (\boldsymbol{p}_3, \boldsymbol{p}_4)$. Scattering rates are computed via the Fermi golden rule taking a repulsive on-site Hubbard-U-type coupling [1] (we fix $U = 2t$), which yields

$$\Gamma^{\text{el-el}}_{\boldsymbol{p}_1 - \boldsymbol{p}_4} \propto U^2 \delta\left(\varepsilon_{\boldsymbol{p}_1} + \varepsilon_{\boldsymbol{p}_2} - \varepsilon_{\boldsymbol{p}_3} - \varepsilon_{\boldsymbol{p}_4}\right) \times \delta(\boldsymbol{p}_1 + \boldsymbol{p}_2 - \boldsymbol{p}_3 - \boldsymbol{p}_4), \tag{5}$$

and satisfies energy as well as momentum conservation. Although the scattering rate is isotropic (s-wave scattering), we find a highly anisotropic contribution to Eq. (4) because of umklapp scattering—the fact that momentum conservation allows for momentum transfer of reciprocal lattice vectors. Indeed, umklapp scattering is the only way for momentum relaxation for the electron-electron collision.

The final ingredient for our calculations is the electron dispersion, which we model after the γ band of Sr_2RuO_4 within a tight-binding description, see Appendix A. In the dispersion, we include the effect of doping and uniaxial strain through the chemical potential and the hopping integrals, respectively. Note that we use a nontrivial Poisson ratio in our calculations, which leads to an asymmetric response to positive and negative uniaxial strains.

To simplify Eq. (1), we use the parametrization [16],

$$f(\boldsymbol{p}) = \left[1 + \exp\left(\frac{\varepsilon(\boldsymbol{p}) - \mu}{T} - \phi(\boldsymbol{p}) \right) \right]^{-1}, \tag{6}$$

which yields in linearized form

$$f(\boldsymbol{p}) \approx f_0(\boldsymbol{p}) + \underbrace{f_0(\boldsymbol{p})[1 - f_0(\boldsymbol{p})]}_{\text{scattering phase space}} \phi(\boldsymbol{p}), \tag{7}$$

with $f_0(\boldsymbol{p})$ as the Fermi-Dirac distribution. The correction $\phi(\boldsymbol{p})$ to be determined, thus, directly relates to the scattering phase space. This correction contains the necessary information to calculate transport coefficients, such as the longitudinal electronic conductivity for an electric-field E along the x axis,

$$\sigma_{xx} = \frac{e}{E} \int (d\boldsymbol{p}) f_0(\boldsymbol{p})[1 - f_0(\boldsymbol{p})]\phi(\boldsymbol{p}) v_x(\boldsymbol{p}), \tag{8}$$

and the longitudinal thermal conductivity for a temperature gradient $T' = (\nabla T)_x$ along the x axis,

$$\kappa_{xx} = \frac{1}{T'} \int (d\boldsymbol{p}) f_0(\boldsymbol{p})[1 - f_0(\boldsymbol{p})]\phi(\boldsymbol{p}) v_x(\boldsymbol{p})(\varepsilon_{\boldsymbol{p}} - \mu). \tag{9}$$

Before solving the full Boltzmann equation including electron-electron scattering numerically in Sec. IV, we first analyze the low-temperature limit where impurity scattering dominates.

III. IMPURITY SCATTERING

Focusing on impurity scattering only, we obtain the linearized Boltzmann equation for $\phi(\boldsymbol{p})$ up to linear order in a constant electric-field $\boldsymbol{E}$ and temperature gradients $\nabla_{\boldsymbol{r}} T$. As shown in Appendix B, the resulting correction reads

$$\phi(\boldsymbol{p}) = -\left[\left(\frac{\varepsilon_{\boldsymbol{p}} - \mu}{T}\right)\nabla_{\boldsymbol{r}} T + e\boldsymbol{E}\right] \cdot \frac{v_{\boldsymbol{p}}}{T} \tau(\varepsilon_{\boldsymbol{p}}). \tag{10}$$

Here, $v_{\boldsymbol{p}} \equiv \dot{\boldsymbol{r}} = \partial_{\boldsymbol{p}} \varepsilon_{\boldsymbol{p}}$ is the velocity, and the effect of impurity scattering appears in the scattering time $\tau(\varepsilon) = \hbar/[2\pi n_{\text{imp}} |v_{\text{imp}}|^2 \Omega N(\varepsilon)]$ with $N(\varepsilon)$ as the density of states at energy ε. Note that, for s-wave scatterers, the scattering time is not direction dependent.

Sufficiently far from the vHS, the density of states $N(\varepsilon) \approx N$ is only weakly depending on energy, resulting in an essentially constant scattering time τ. Therefore, we recover the well-known scattering-time approximation [17],

$$f_{\boldsymbol{E}}(\boldsymbol{p}) \approx f_0\left(\boldsymbol{p} + \frac{e\tau}{\hbar}\boldsymbol{E}\right), \tag{11}$$

$$f_{\nabla T}(\boldsymbol{p}) \approx \frac{1}{1 + \exp\left(\frac{\varepsilon_{\boldsymbol{p}} - \mu}{T - \tau v \cdot \nabla T}\right)}. \tag{12}$$

As we approach the vHS, we find that $\phi(\boldsymbol{p})$ vanishes for all directions of $\boldsymbol{p}$ since $\tau(\varepsilon) \propto 1/N(\varepsilon) \to 0$. Thus, we expect for both types of Lifshitz transitions a qualitatively similar behavior, namely, a suppression in all directions due to the vanishing scattering time. Physically, the large scattering phase space available at energies near the vHS leads to a fast momentum relaxation such that an applied field or temperature gradient can shift the Fermi distribution only weakly. Note that this effect is naturally weaker in the case of a Lifshitz transition at only one van Hove point as realized by uniaxial strain.

For a qualitative understanding of electrical transport at low temperatures and Fermi energy near a vHS, we use

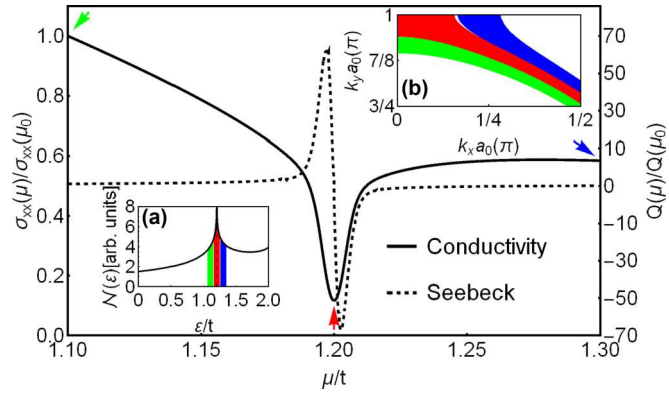

FIG. 2. Conductivity dip due to enhanced impurity scattering together with the switching sign of the Seebeck coefficient near the Lifshitz point normalized to the undoped resistivity $\mu_0 = 1.1t$. Inset (a) shows the density of states together with the energy intervals of the contributing states for $\mu/t = 1.1$ (green), $\mu/t = 1.2$ (red), and $\mu/t = 1.3$ (blue). Inset (b) shows the contributing states for these three cases for the scattering phase-space $f_0(\mathbf{p})[1 - f_0(\mathbf{p})] \leqslant 10^{-10}$.

Eq. (10) to obtain the conductivity through Eq. (8),

$$\sigma_{xx} = \frac{e^2}{T} \int (d\boldsymbol{p}) f_0(\boldsymbol{p})[1 - f_0(\boldsymbol{p})]\tau(\varepsilon_{\boldsymbol{p}}) \left(v_{\boldsymbol{p}}^x\right)^2 \tag{13}$$

$$= \frac{e^2}{T} \int d\varepsilon\, f_0(\varepsilon)[1 - f_0(\varepsilon)]\tau(\varepsilon) \left\langle \frac{\left(v_{\boldsymbol{p}}^x\right)^2}{|\nabla_{\boldsymbol{p}} \varepsilon_{\boldsymbol{p}}|} \right\rangle_{\varepsilon}, \tag{14}$$

where we have introduced the equal-energy-contour average $\langle A \rangle_{\varepsilon} = \int_{\varepsilon_{\boldsymbol{p}} = \varepsilon} (d\boldsymbol{p}) A$. For $T \to 0$, this integral is dominated by $\varepsilon = \varepsilon_F$, the Fermi energy such that

$$\sigma_{xx} \approx e^2 \tau(\varepsilon_F) \left\langle \frac{\left(v_{\boldsymbol{p}}^x\right)^2}{|v_{\boldsymbol{p}}|} \right\rangle_{\varepsilon_F}, \tag{15}$$

where $\langle \cdot \rangle_{\varepsilon_F}$ denotes a Fermi-surface average. As noted above, the suppression of the scattering time $\tau(\varepsilon_F)$ close to the vHS leads to a reduction of the conductivity. Figure 2 shows the corresponding dip in the longitudinal conductivity by evaluating Eq. (13) together with the Seebeck coefficient approximated through Mott's formula,

$$Q = -\frac{\pi^2}{3} \frac{k_B^2 T}{e} \frac{\sigma'(\varepsilon)}{\sigma(\varepsilon)}\bigg|_{\varepsilon = \mu}, \tag{16}$$

considering the doping scenario at a low-temperatures ($T/t \sim 10^{-3}$). Note that the shown conductivity is already in good qualitative agreement with the experimental findings of Refs. [8,10].

An interesting feature arises for the case where uniaxial strain pushes the Fermi surface through van Hove points at $\boldsymbol{k} = (0, \pi)$ corresponding to negative ε_{xx} in Fig. 1(b). In this case, the averages over the energy contours in Eq. (14) are dominated by the momentum direction along [1,0]. For $T = 0$, the conductivity vanishes for $\varepsilon_{xx} = \varepsilon_{\text{vH}}$ according to Eq. (15) due to the vanishing scattering time. Once the temperature increases, the range of energy averaging grows such that with τ also the conductivity becomes finite and grows with increasing temperature. Although upon uniaxial deformation

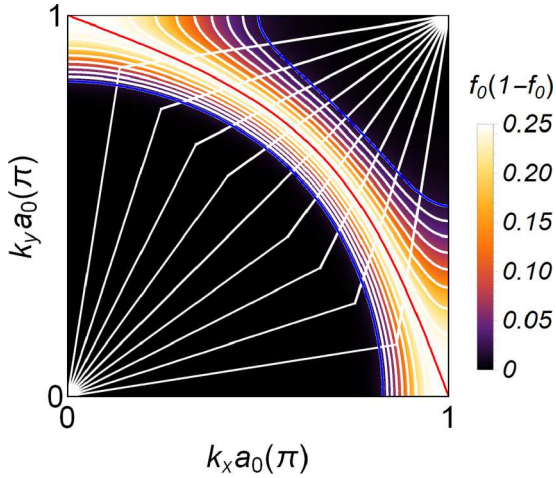

FIG. 3. Discretization of the first BZ adapted to the scattering phase space. The red curve corresponds to the Fermi-surface crossing the vHS. Blue curves denote the boundary equipotentials of the discretization, i.e., $\varepsilon_F - 4T$ and $\varepsilon_F + 4T$. Note that, for demonstration purposes, a high temperature of ∼100 K is shown.

($\varepsilon_{xx} < 0$) the Fermi surface along [0,1] passes through the vHS, it retreats from the van Hove point along [1,0] due to Luttinger's theorem. Therefore, the Fermi velocity v_F^x along [1,0] increases monotonically with increasing deformation. Since the scattering time τ is an approximately symmetric function of $\varepsilon_{xx} - \varepsilon_{\mathrm{vH}}$ with its minimum at $\varepsilon_{xx} = \varepsilon_{\mathrm{vH}}$, the ε_{xx} dependence of the average of $\langle (v_p^x)^2/|v_p|\rangle_\varepsilon$ leads to a shift of the minimum towards $\varepsilon_{xx} < \varepsilon_{\mathrm{vH}}$ for increasing temperature. This behavior agrees well with the numerical solution of the linearized Boltzmann equations presented in the next section and reproduces also the qualitative behavior observed in experiments [8]. For the opposite situation of positive uniaxial strain $\varepsilon_{xx} > 0$, this argument does not apply, and we will see below that there is no temperature-dependent shift of the conductance minimum.

IV. NUMERICAL RESULTS

We now turn to the numerical solution of the linearized Boltzmann Eq. (1), including both impurity and electron-electron scattering. Our calculation includes the full momentum dependence of the scattering terms and, thus, goes beyond the relaxation-time approximation. The most important part of momentum space for this calculation is close to the Fermi surface representing the scattering phase space. Thus, we adopt the discretization scheme from Ref. [18] shown in Fig. 3 with momentum space patches following band energy equipotential lines distributed between $\varepsilon_F - 4T$ and $\varepsilon_F + 4T$ together with equally distributed angular ϑ coordinates. An advantage of our technique is that the patched discretization of the BZ is adaptive to the temperature. In other words, we always work with the same number of patches regardless of the temperature. Note that we normalize the temperature scale with respect to $t = 0.14$ eV [19] in order to compare with experimental results.

We use a sufficiently dense set of angular (ϑ) and energy (ε) contours, namely, 160 angular and 30 energy contours to ensure high accuracy. A high-resolution discretization is particularly important for the calculation of the electron-electron collision integral Eq. (4) and its anisotropy due to umklapp processes [1] where the relevant phase space is located around the crossing points of the Fermi surfaces and the umklapp zones denoted in Fig. 1. We distinguish two umklapp processes, one for reciprocal lattice vectors $(2\pi, 0)$ and $(0, 2\pi)$ corresponding to the boundaries of the dark blue zones in Fig. 1 and the $(2\pi, 2\pi)$ indicated by the white diamond-shaped boundary. Only such high resolution allows us to analyze the subtle low-temperature dependence of transport quantities which are strongly influenced by the position of the Fermi-surface crossings. Only when we generate maps (and low-temperature details) of quantities, such as shown in Figs. 4(e) and 4(f) do we reduce the angular resolution to 40 contours for performance reasons. This resolution is sufficient in these cases to provide information on temperature dependence of the displayed quantities.

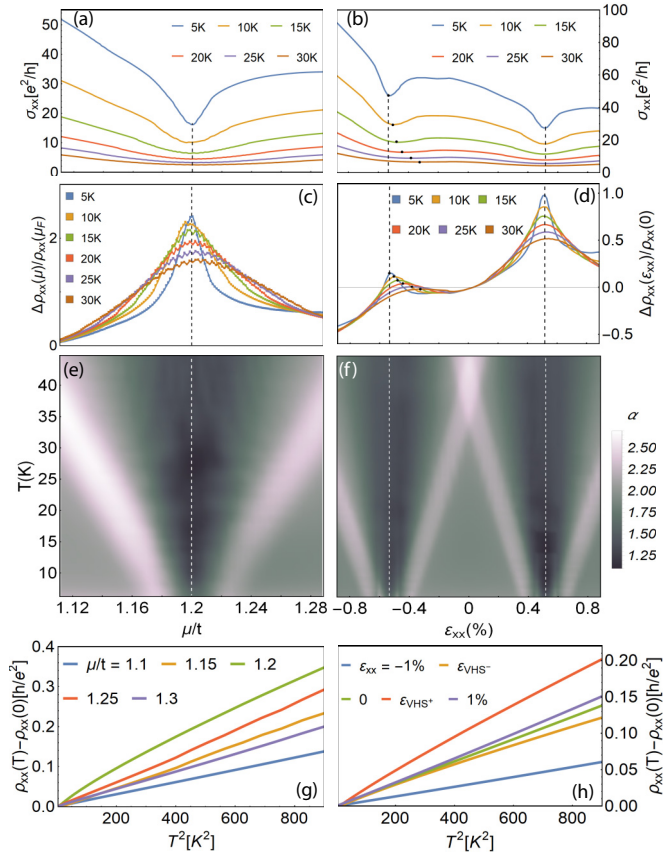

FIG. 4. Summary of numerical results for the electronic transport: Temperature evolution of the conductivity [(a) and (b)], normalized resistivity [(c) and (d)], temperature scaling coefficient α [(e) and (f)], as well as resistivity curves for various values of μ/t and ε_{xx} comparing band filling (left panel) and uniaxial strain (right panel) scenarios. Subfigures (g) and (h) correspond to temperature cuts of the resistivity at values of interesting band fillings and values of uniaxial strains. Note the strongly nonlinear temperature dependence of $\rho_{xx}(T^2)$ considering $\mu/t = 1.2$ [green curve in subfigure (g)] and similar dependence at both Lifshitz points $\varepsilon_{vHS^\pm}$ [orange and red curves in subfigure (h)].

A. Electrical transport

Figure 4 provides an overview of our main numerical results for the electrical conductivity σ_{xx} for the two cases of Fermi-surface tuning using the full solution to Eq. (1). The upper six panels provide scans of the tuning parameter μ for the case of doping on the left-hand side and ε_{xx} for uniaxial deformation on the right-hand side. The Lifshitz transitions occur at $\mu = 1.2t$ and $\varepsilon_{xx} = \varepsilon_{\mathrm{vH}} \sim \pm 0.53\%$. Panels (a) and (b) display the conductivity with dips, which become more pronounced with decreasing temperature, at the Lifshitz transitions. The shift of the minimum away from the Lifshitz-transition point in the case of $\varepsilon_{xx} < 0$ is marked by dots in panel (b). Panels (c) and (d) show the relative change in the resistivity $\Delta\rho_{xx}(\mu) = \rho_{xx}(\mu) - \rho_{xx}(\mu_F)$ normalized with respect to $\rho_{xx}(\mu_F)$, where $\mu_F = 1.1t$ is the chemical potential of the undoped case and $\Delta\rho_{xx}(\varepsilon) = \rho_{xx}(\varepsilon) - \rho_{xx}(0)$ normalized with respect to $\rho_{xx}(\varepsilon_{xx} = 0)$. In both cases, the dips in σ_{xx} translate to peaks whose maxima grow with decreasing temperature. Note that, for $\varepsilon_{xx} < 0$, the resistivity, including the shift of the maxima, resembles qualitatively very well the experimental results found in Ref. [8].

We turn to the low-temperature behavior of ρ_{xx}, which we use as our first tool to identify deviations from the standard Fermi-liquid picture. The temperature dependence of the resistivity as displayed in panels (g) and (h) can be fitted by

$$\rho_{xx}(T) = \rho_0 + AT^{\alpha}, \tag{17}$$

with the parameters A and α besides the residual resistivity ρ_0. The exponent $\alpha = 2$ denotes a Fermi liquid, whereas α smaller than 2 is considered as non-Fermi-liquid behavior. We determine the exponent from the numerical results using

$$\alpha = \frac{\partial \ln[\rho(T) - \rho(0)]}{\partial \ln T}, \tag{18}$$

which yields the α maps in panels (e) and (f). In both cases, we see triangle-shaped regions with $\alpha \approx 2$ far enough from the Lifshitz points. On the other hand, at the Lifshitz transition, a fan of values α clearly smaller than two opens. The two regimes are separated by bright stripes ($\alpha > 2$), which result from Eq. (18) when ρ_{xx} has a kinklike feature as the vHS enters the scattering phase space upon increasing the temperature. These kinks are visible by eye in the plots of ρ_{xx} in panel (g) for $\mu/t = 1.15$ and 1.25.

B. Kadowaki-Woods ratio

In the Fermi-liquid regime ($\alpha = 2$), the fitting parameter A in Eq. (17) can be used together with the Sommerfeld coefficient $\gamma \propto N(\varepsilon_F)$ to define the Kadowaki-Woods ratio $R_{\mathrm{KW}} = A/\gamma^2$. This ratio is empirically a material-independent constant for several material classes [20] and has been suggested to remain constant if the strength of the electron correlations varies for a fixed bare band structure [21]. In their experiments with uniaxially deformed Sr_2RuO_4, Barber *et al.* [8] observed an increase in A faster than that of γ^2, anticipated from DFT calculations, upon tuning the Fermi surface towards the vHS for $\varepsilon_{xx} < 0$. In order to analyze this behavior, we determine A and R_{KW} within our approach by fitting the resistivity curves to a quadratic behavior $\rho(T) = \rho_0 + AT^2$ where applicable, and we calculate γ from our tight-binding band structure. Figure 5 shows both A and R_{KW} in the low-temperature regime, where $\alpha = 2$ indicates Fermi-liquid-like behavior. We find that A increases as the Fermi surface shifts towards the vHS and indeed faster than γ^2 such that the Kadowaki-Woods ratio also increases in a similar way. Note that the behavior we find for A considering $\varepsilon_{xx} < 0$ in panel (b) is in good qualitative agreement with the experimental findings [8].

C. Thermal transport and Seebeck coefficient

The electronic contribution to the thermal transport can be calculated numerically in a manner analogous to the electrical conductivity in the previous section. Figures 6(a) and 6(b) show the thermal conductivity κ_{xx}, which exhibits similar features as the conductivity σ_{xx} presented in Fig. 4, including, in particular, the dips at the Lifshitz transitions. These dips are naturally wider because the integral for the thermal conductivity,

$$\kappa_{xx} = \frac{1}{T'} \int (d\boldsymbol{p}) f(\boldsymbol{p}) v_{\boldsymbol{p}}^{x} [\varepsilon(\boldsymbol{p}) - \mu] \tag{19}$$

contains also the electron dispersion which is essentially flat at the vHS. A further difference is the weaker temperature dependence of the minima. However, there is again a temperature-dependent shift of the minimum position for uniaxial strain $\varepsilon_{xx} < 0$ as observed and discussed for σ_{xx} [see Fig. 4(b)].

The Seebeck coefficient Q relates a temperature gradient to a resulting electric field $\boldsymbol{E} = Q\boldsymbol{\nabla} T$ under an open circuit condition and follows from the solution to the linearized Boltzmann equation. It is given by

$$Q = \frac{|\boldsymbol{E}|}{e|\boldsymbol{\nabla} T|} \frac{\int (d\boldsymbol{p}) v_{\boldsymbol{p}}^{x} f_0(\boldsymbol{p})[1 - f_0(\boldsymbol{p})] \tilde{\phi}_{\boldsymbol{\nabla} T}(\boldsymbol{p})}{\int (d\boldsymbol{p}) v_{\boldsymbol{p}}^{x} f_0(\boldsymbol{p})[1 - f_0(\boldsymbol{p})] \tilde{\phi}_{\boldsymbol{E}}(\boldsymbol{p})}, \tag{20}$$

where $\tilde{\phi}_{\boldsymbol{E}}$ and $\tilde{\phi}_{\boldsymbol{\nabla} T}$ correspond to the solution of the Boltzmann equation with only external electric-field $\boldsymbol{E}$ or temperature gradient $\boldsymbol{\nabla} T$. We can use the Seebeck coefficient as a second tool to identify deviations from Fermi-liquid behavior, since for a Fermi liquid, Q has linear temperature dependence. For this reason, we plot the ratio Q/T in Figs. 6(c) and 6(d) as a map of temperature versus chemical potential and strain. We again recognize different regimes where the umklapp processes are clearly observable in both panels. In panels (e) and (f), we focus on the low-temperature regime and show Q/T scans for fixed temperatures. We find little temperature dependence away from the Lifshitz points in accordance with expectations for Fermi liquids. Around the Lifshitz points, on the other hand, anomalies emerge with lowering temperature including a sign change. Interestingly, this agrees well with the Mott formula given by Eq. (16) considering the case of tuning by chemical potential. The dip in conductance results in a sign change with the anomalies corresponding to the inflection points of $\sigma_{xx}(\mu)$. The reason for this agreement lies in the disappearance of the highly anisotropic contribution of electron-electron scattering to momentum relaxation at

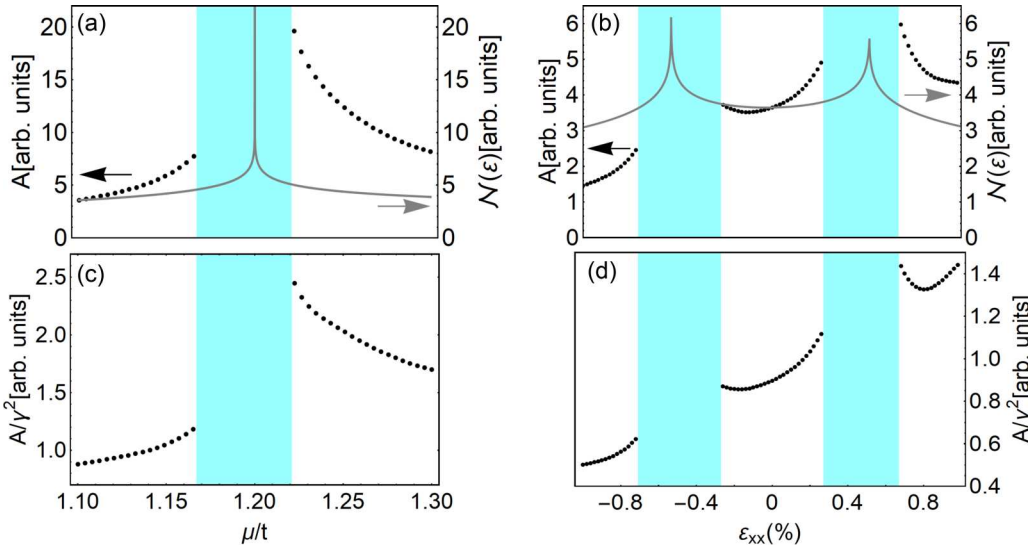

FIG. 5. Coefficient A extracted by fitting the data used in Fig. 4 of $\rho(T) = \rho_0 + AT^2$ [subfigures (a) and (b)] together with the Kadowaki-Woods ratio $R_{\mathrm{KW}} = A/\gamma^2$ [subfigures (c) and (d)] as a function of band filling (left panel) and uniaxial strain (right panel). In the colored regions, fitting α yields a result $\notin [1.9, 2.1]$, which we consider non-Fermi-liquid-like. Note that, outside of these regions, the density of states at the Fermi level (gray lines) remains almost constant.

low temperatures. At higher temperatures, these anisotropies change the behavior of Q/T rather profoundly [16,22]. The same argument applies also to the case of Fermi-surface tuning by uniaxial strain where, near the Lifshitz point, the Mott formula can be approximated by

$$Q \propto -\frac{1}{\sigma(\varepsilon_{xx})}\frac{\partial\sigma(\varepsilon_{xx})}{\partial|\varepsilon_{xx}|}. \tag{21}$$

Thus, a change in ε_{xx} has an analogous effect as a variation of the chemical potential, justifying this approximation.

D. Wiedemann-Franz law

The anisotropy of scattering due to umklapp processes affects the electrical and thermal conductances in a different way. This impacts the temperature dependence of both as well as the Wiedemann-Franz law. The Lorenz number, defined as

$$L(T) = \frac{\kappa_{xx}(T)}{T\sigma_{xx}(T)} \tag{22}$$

is constant and given by $L_0 = \pi^2 k_B^2/3e^2$ for isotropic scattering. In Fig. 7, we display the ratio $L(T)/L_0$ for a range of varying band fillings [(a)] and uniaxial deformation [(b)] including the Lifshitz transitions. A general observation is

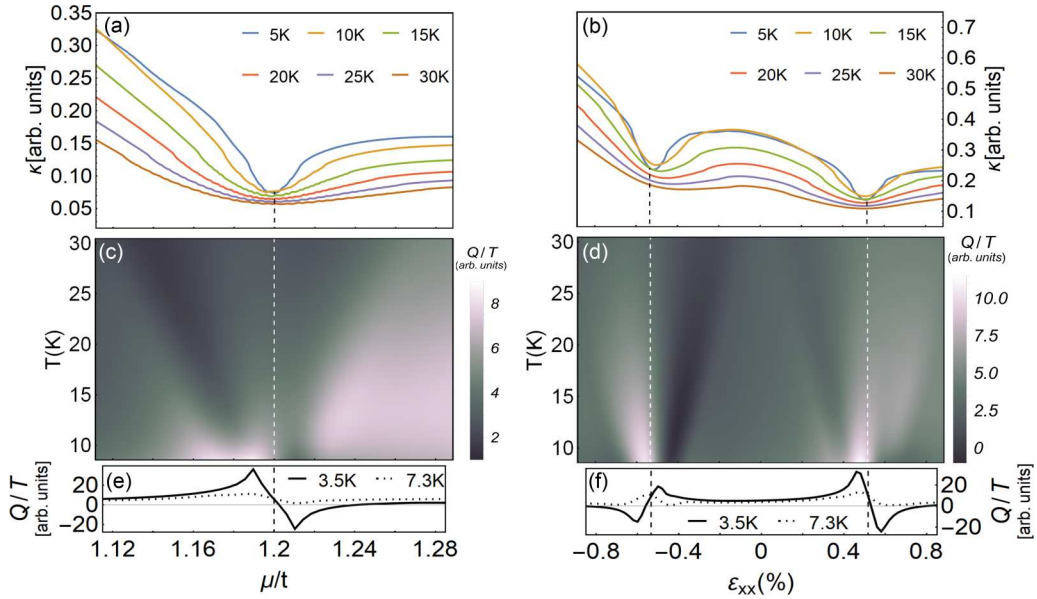

FIG. 6. Temperature evolution of the thermal conductivity [(a) and (b)] as well as the Seebeck coefficient divided by the temperature Q/T [(c) and (d)] together with the detail at the low-temperature Q/T [(e) and (f)] comparing the band filling and the uniaxial-strain scenarios.

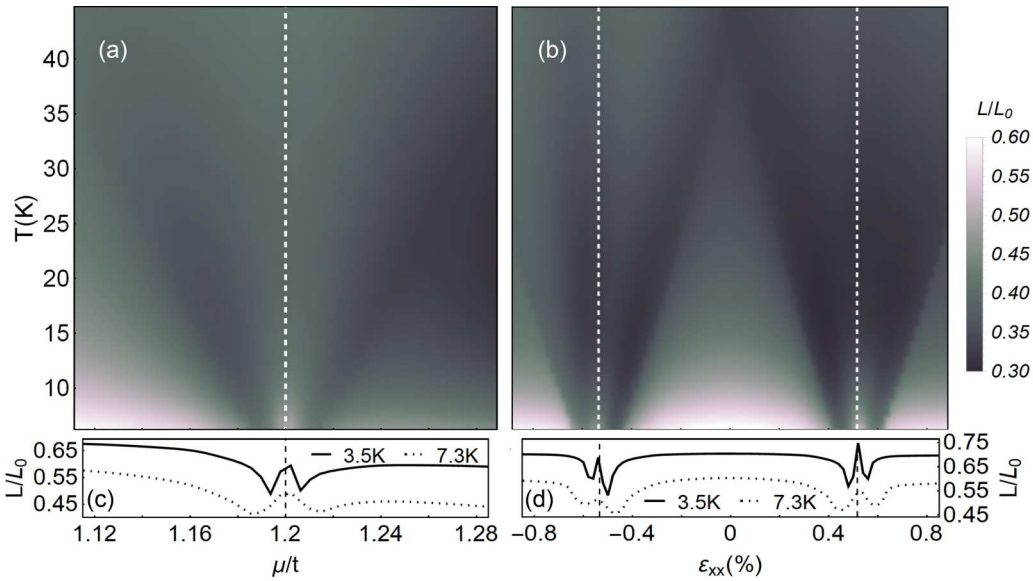

FIG. 7. Deviations from the Wiedemann-Franz law as a function of band filling (left panel) and uniaxial strain (right panel). The dashed lines mark the Lifshitz transitions.

that, $L < L_0$, signaling that the thermal transport is more efficiently impeded by scattering here than the charge transport. In the regions far from the Lifshitz transitions, which we identified previously as the (triangle-shaped) Fermi-liquid regime, L/L_0 is larger and additionally increases as temperature decreases such that L approaches L_0. This indicates that electron-electron scattering is responsible for the suppression of L, whereas isotropic impurity scattering leads to a higher value of L. Notable is the difference between the Fermi-liquid regions for $\mu < 1.2t$ and $\mu > 1.2t$ in Fig. 7(a). Although, in the former case, both umklapp processes, involving the reciprocal lattice vectors of the kind of $(2\pi, 0)$ and $(2\pi, 2\pi)$, are allowed, in the latter case only the $(2\pi, 0)$ type of umklapp contributes and leads to a more pronounced anisotropy. At the same time, the electron density, which increases with the chemical potential, increases the scattering probability. This leads to a stronger suppression of L than in the range of $\mu < 1.2t$. In contrast, the Fermi-liquid regimes for a uniaxial deformation are fairly comparable in their behavior, and the whole picture looks rather symmetric around ε_{xx}.

In the vicinity of the Lifshitz points, we observe a pronounced drop of L/L_0, whose onset is temperature dependent and can be identified by the overlap of the scattering phase space with the vHS. This enlarged phase space is accompanied by more electronic states contributing to energy transport. This is supported by the observation that, comparing Figs. 4(a) and 4(b) with Figs. 6(a) and 6(b), the dips in the conductivity are sharper in the former than in the latter case. This gives rise to the strong reduction of L. Right at the Lifshitz point, on the other hand, we find a very narrow region where L recovers for very low temperatures. This effect is due to the weak-temperature dependence of the minima values for κ_{xx}, in contrast to the strong decrease in σ_{xx} with lowering T.

To summarize, the Lorenz number deviates rather strongly from the Wiedemann-Franz value of L_0 as a consequence of the rather complex scattering behavior encountered in our system. This deviation shows further pronounced features through the special scattering properties close to the Lifshitz transition.

E. Hall resistivity

The Hall resistivity $R_H = \sigma_{xy}/B_z(\sigma_{xx}^2 + \sigma_{xy}^2)$—we set the magnetic field along z, and the current flow along the x axis is used to characterize the nature of the charge carriers. It is interesting to follow the evolution of R_H in the two cases of Fermi-surface change. In Fig. 8, we display the result for R_H from the numerical solution of the Boltzmann equations including an out-of-plane magnetic field [16]. There is a large difference between the Fermi-surface tuning by band filling [(a)] and the uniaxial deformation [(b)] considering the magnitude: For the latter tuning, the effect is an order of magnitude larger in the considered range of tuning parameters. The sign change in R_H, Fig. 8(a), reflects the change from an electron- to a holelike Fermi surface with a strong temperature dependence of the zero-crossing point. Even at the lowest temperature, however, the sign change in R_H is not exactly at the Lifshitz transition.

In fact, the current density along the x direction yields the dominant modification of the Fermi distribution along [1,0]. The sign of R_H is determined by the curvature of the Fermi-surface region, which dominantly carries the current. Looking at Fig. 1(a), the curvature at the Lifshitz transition is convex and yields an electronlike behavior of R_H. Only raising the chemical potential μ higher leads to the emergence of dominantly concave curvature around the [1,0] direction and, thus, to the sign change in R_H at $\mu \approx 1.25t$ for $T = 5$ K. For higher temperatures, this feature shifts to lower μ due to thermal smearing of the Fermi-surface region.

For the Fermi surface tuned by uniaxial deformation, Fig. 8(b), the sign of R_H is opposite for positive and negative strains if the temperature is sufficiently high, a behavior which becomes more pronounced with growing T. For the lowest temperature displayed, however, R_H is strictly negative.

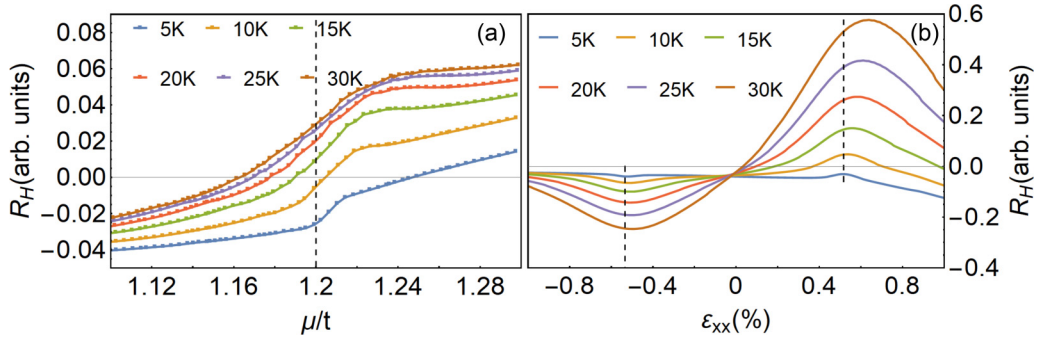

FIG. 8. Temperature dependence of the Hall resistivity for the band-filling as well as the uniaxial-strain scenarios. The line at $R_H = 0$ denotes where the character of the charge-carrier changes.

Again, we may consider the curvature of the current-carrying parts for the Fermi surface. For $\varepsilon_{xx} < 0$, the Fermi surface around the [1,0] direction remains convex, in other words, electronlike such that $R_H < 0$. For the other strain direction, the curvature is concave only in a small part near the vHS, which, due to its orientation (with the normal vector dominantly along the [0,1] direction), contributes only weakly to the current density. The major contribution to the current density originates from the convex Fermi-surface parts with Fermi velocities of sizable x component, as can be anticipated from Fig. 1(b). In this case, however, increasing temperature yields a Fermi-surface smearing which yields an effective curvature analogous to the situation we observed in the case of varying chemical potential. The extrema of R_H at the two Lifshitz transitions and their increase are caused by the dips of σ_{xx} which appear quadratically in the denominator of R_H and the strong temperature dependence.

To our knowledge there are no Hall effect measurements for any of the investigated situations. It would indeed be a helpful test for the quasiparticle picture and our approach to be able to have a comparison with experiments.

V. CONCLUSIONS

Our analytical and, in particular, numerical investigations of transport properties in a single-band model with a Fermi surface undergoing a Lifshitz transition display a complex behavior. Our numerical scheme allows us to take the highly anisotropic structure of the electron-electron scattering with umklapp processes into account. In combination with simple isotropic impurity scattering, we find that the electrical resistivity strongly deviates from the standard Fermi-liquid picture, although our starting point relies on the integrity of the quasiparticle description.

Although our paper is motivated by experiments on Sr_2RuO_4, which possesses three bands at the Fermi level, we focused on a single-band picture including the γ band only. The α and β bands correspond to hybridized quasi-one-dimensional bands and are only weakly affected by the tuning parameters we have used. In particular, their Fermi surfaces never approach the van Hove points in the BZ. Thus, the single-band approximation can be justified on a qualitative level since, near the Lifshitz transitions, the γ band is expected to dominate the anomalous transport properties on top of a background coming from regular parts of the Fermi surface. Nevertheless, in order to obtain a more quantitative picture, all bands should be considered. Moreover, scattering vertex corrections may yield important corrections which have not been taken into account here [18]. These extensions are referred to future studies.

Although a standard perturbation picture [17] of the shifted Fermi surface due to an external electric field fails in the vicinity of the Lifshitz point, our semianalytical and numerical approach to the solution of the Boltzmann transport equation and the comparison with experiment indicates that a quasiparticle description may indeed be used throughout the whole range of Fermi-surface tuning including the Lifshitz points. Analyzing different transport properties, we see that the electron-electron scattering yields strong modifications due to the high anisotropy introduced by umklapp processes. These processes act in a restricted phase space, which is rather strongly temperature dependent. The considered (noninvasive) Fermi-surface tuning allows to modify this umklapp phase space and to probe its impact on transport properties. These include not only the electrical conductivity, but also the thermal conductivity, the Seebeck coefficient, and, in a more indirect way, the Hall effect. Our predictions of these general transport properties for the two different Fermi-surface-tuning possibilities allow for further experimental scrutiny of the quasiparticle picture for both charge and heat transports and thus, of the electronic nature of a system close to a van Hove singularity.

ACKNOWLEDGMENTS

We would like to thank C. Hicks and A. Mackenzie for many valuable discussions. We gratefully acknowledge financial support by the Swiss National Science Foundation through Division II (Grant No. 163186).

APPENDIX A: MODEL FOR THE γ BAND OF Sr_2RuO_4

We approximate the γ band, including the effect of uniaxial stress, but a two-dimensional nearest- and next-nearest-neighbor tight-binding model,

$$\varepsilon_{\mathbf{k}} = -2[t_x \cos(k_x a) + t_y \cos(k_y b)] - 2t'[\cos(k_x a + k_y b) + \cos(k_x a - k_y b)]. \quad \text{(A1)}$$

Note that, in the main text, we use the momentum $\boldsymbol{p} = \hbar\mathbf{k}$. For the implementation of the band tuning by uniaxial strain, we

follow Ref. [8] to and describe the deformation of the unit cell for the lattice constants a and b along the x and y directions, respectively, by

$$a(\varepsilon_{xx}) = a_0(1+\varepsilon_{xx}), \qquad b(\varepsilon_{yy}) = a_0(1+\varepsilon_{yy}),$$

where ε_{xx} and ε_{yy} are the strain components along the two main axes. For given applied stress σ_{xx} along the x direction the two strain components are connected via the Poisson ratio ν_{xy}: $\varepsilon_{yy} = \nu_{xy}\varepsilon_{xx}$ with $\nu_{xy} < 0$ and $\sigma_{xx} = E\varepsilon_{xx}$ (E: Young's elasticity modulus). The lattice deformation modifies of the hopping integrals linearly in the strain,

$$t_x(\varepsilon_{xx}) = t_0(1-\alpha\varepsilon_{xx}), \qquad t_y(\varepsilon_{xx}) = t_0(1+\alpha\nu_{xy}\varepsilon_{xx})$$
$$t'(\varepsilon_{xx}) = t_0'[1-\alpha(1-\nu_{xy})\varepsilon_{xx}/2],$$

where α is a constant parameter adjusting the scale of the effect of the strain.

For numerical calculations, we use the hopping matrix elements $t_0/t = 0.8$, $t_0'/t = 0.3$, the bare chemical potential $\mu_0/t = 1.1$, $\alpha = 10$, and $\nu_{xy} = -0.39$, where $t = 0.14$ eV is the nearest-neighbor-hopping strength of the α band of Sr_2RuO_4 grown on $SrTiO_3$ [19]. For the Hall resistivity, we use a magnetic field in the dimensionless units $\mathcal{B}_z = (2\pi)^3\frac{ea^2}{\hbar}B_z$ with the value of $\mathcal{B}_z = 0.1$.

APPENDIX B: LINEARIZED BOLTZMANN EQUATION FOR IMPURITY SCATTERING

Here, we derive the linearized Boltzmann equation for small external electric-fields $\boldsymbol{E}$ and temperature gradients $\nabla_r T(\boldsymbol{r})$.

1. Collision integral

First, we calculate the impurity-scattering collision integral Eq. (2) for isotropic point scattering centers with Eq. (3) to lowest order in the correction to the Fermi-Dirac distribution $f_0(\boldsymbol{p})$. Using the expansion of Eq. (7) and $f_0(\boldsymbol{p}) = f_0(\varepsilon_{\boldsymbol{p}})$, we find

$$[\partial_t f(\boldsymbol{p})]_{\rm imp} = -\Omega n_{\rm imp} v_{\rm imp}^2 \frac{2\pi}{\hbar}\int (d\boldsymbol{p}')\delta(\varepsilon_{\boldsymbol{p}}-\varepsilon_{\boldsymbol{p}'}) \times f_0(\varepsilon_{\boldsymbol{p}})[1-f_0(\varepsilon_{\boldsymbol{p}})][\phi(\boldsymbol{p})-\phi(\boldsymbol{p}')]. \quad \text{(B1)}$$

We can further simplify this expression to

$$[\partial_t f(\boldsymbol{p})]_{\rm imp} = -\Omega n_{\rm imp} v_{\rm imp}^2 \frac{2\pi}{\hbar} f_0(\varepsilon_{\boldsymbol{p}})[1-f_0(\varepsilon_{\boldsymbol{p}})] \times \int_{\varepsilon_{\boldsymbol{p}}=\varepsilon_{\boldsymbol{p}'}} \frac{(d\boldsymbol{p}')}{|\nabla\varepsilon_{\boldsymbol{p}'}|}[\phi(\boldsymbol{p})-\phi(\boldsymbol{p}')]. \quad \text{(B2)}$$

Using the fact that $\phi(\boldsymbol{p}')$ is an odd function of $\boldsymbol{p}'$, only the first contribution in Eq. (B2) survives, and introducing the density of states $N(\varepsilon) = \int_{\varepsilon_{\boldsymbol{p}'}=\varepsilon}(d\boldsymbol{p}')/|\nabla\varepsilon_{\boldsymbol{p}'}|$, we find the linearized collision integral,

$$[\partial_t f(\boldsymbol{p})]_{\rm imp} = -\underbrace{\frac{2\pi\,\Omega n_{\rm imp} v_{\rm imp}^2 N(\varepsilon_{\boldsymbol{p}})}{\hbar}}_{\tau(\varepsilon_{\boldsymbol{p}})^{-1}} f_0(\varepsilon_{\boldsymbol{p}})[1-f_0(\varepsilon_{\boldsymbol{p}})]\phi(\boldsymbol{p}). \quad \text{(B3)}$$

As expected, for point scattering centers, the scattering time is angle independent (s-wave scattering).

2. Temperature gradient and external electric field

Introducing $v_{\boldsymbol{p}} \equiv \dot{\boldsymbol{r}} = \nabla_{\boldsymbol{p}}\varepsilon_{\boldsymbol{p}}$, we can write the second term of the left-hand side of Eq. (1) to lowest order as

$$\dot{\boldsymbol{r}}\cdot\nabla_{\boldsymbol{r}} f(\boldsymbol{p}) = v_{\boldsymbol{p}}\cdot\nabla_{\boldsymbol{r}} f(\boldsymbol{u}) \quad \text{(B4)}$$
$$= f_0(\varepsilon_{\boldsymbol{p}})[1-f_0(\varepsilon_{\boldsymbol{p}})]\left(\frac{\varepsilon_{\boldsymbol{p}}-\mu}{T^2}\right)\nabla_{\boldsymbol{r}} T(\boldsymbol{r})\cdot v_{\boldsymbol{p}}. \quad \text{(B5)}$$

Furthermore, we calculate the third term on the left-hand side of Eq. (1). Considering only an electric field, i.e., $\dot{\boldsymbol{p}} = -e\boldsymbol{E}$, this yields to lowest order in the applied field $\boldsymbol{E}$,

$$\dot{\boldsymbol{p}}\cdot\nabla_{\boldsymbol{p}} f(\boldsymbol{p}) = -e\boldsymbol{E}\cdot\nabla_{\boldsymbol{p}} f(\boldsymbol{p}) \quad \text{(B6)}$$
$$= -e\frac{\boldsymbol{E}\cdot v_{\boldsymbol{p}}}{T} f_0(\boldsymbol{p})[1-f_0(\boldsymbol{p})]. \quad \text{(B7)}$$

Using Eqs. (B3), (B7), and (B4) we find the linearized Boltzmann equation,

$$[\partial_t + \tau(\varepsilon_{\boldsymbol{p}})^{-1}]\phi(\boldsymbol{u}) = -\left[\left(\frac{\varepsilon_{\boldsymbol{p}}-\mu}{T}\right)\nabla_{\boldsymbol{r}} T(\boldsymbol{r}) + e\boldsymbol{E}\right]\cdot\frac{v_{\boldsymbol{p}}}{T}, \quad \text{(B8)}$$

which finally leads to the stationary solution,

$$\phi(\boldsymbol{p}) = -\left[\left(\frac{\varepsilon_{\boldsymbol{p}}-\mu}{T}\right)\nabla_{\boldsymbol{r}} T(\boldsymbol{r}) + e\boldsymbol{E}\right]\cdot\frac{v_{\boldsymbol{p}}}{T}\tau(\varepsilon_{\boldsymbol{p}}). \quad \text{(B9)}$$

[1] J. M. Buhmann, Phys. Rev. B **88**, 245128 (2013).
[2] C. W. Hicks, D. O. Brodsky, E. A. Yelland, A. S. Gibbs, J. A. N. Bruin, M. E. Barber, S. D. Edkins, K. Nishimura, S. Yonezawa, Y. Maeno, and A. P. Mackenzie, Science **344**, 283 (2014).
[3] D. R. Overcash, T. Davis, J. W. Cook, and M. J. Skove, Phys. Rev. Lett. **46**, 287 (1981).
[4] C. L. Watlington, J. W. Cook, and M. J. Skove, Phys. Rev. B **15**, 1370 (1977).
[5] U. Welp, M. Grimsditch, S. Fleshler, W. Nessler, J. Downey, G. W. Crabtree, and J. Guimpel, Phys. Rev. Lett. **69**, 2130 (1992).
[6] Y. Maeno, K. Yoshida, H. Hashimoto, S. Nishizaki, S.-i. Ikeda, M. Nohara, T. Fujita, A. P. Mackenzie, N. E. Hussey, J. G. Bednorz, and F. Lichtenberg, J. Phys. Soc. Jpn. **66**, 1405 (1997).
[7] C. Bergemann, A. P. Mackenzie, S. R. Julian, D. Forsythe, and E. Ohmichi, Adv. Phys. **52**, 639 (2003).
[8] M. E. Barber, A. S. Gibbs, Y. Maeno, A. P. Mackenzie, and C. W. Hicks, Phys. Rev. Lett. **120**, 076602 (2018).
[9] I. M. Lifshitz, J. Exptl. Theoret. Phys. (U.S.S.R.) **38**, 1569 (1960).
[10] B. Burganov, C. Adamo, A. Mulder, M. Uchida, P. D. C. King, J. W. Harter, D. E. Shai, A. S. Gibbs, A. P. Mackenzie, R.

Uecker, M. Bruetzam, M. R. Beasley, C. J. Fennie, D. G. Schlom, and K. M. Shen, Phys. Rev. Lett. **116**, 197003 (2016).
[11] A. Varlamov and A. Pantsulaya, Zh. Eksp. Teor. Fiz. **89**, 2188 (1985).
[12] A. Varlamov, V. Egorov, and A. Pantsulaya, Adv. Phys. **38**, 469 (1989).
[13] Y. Blanter, M. Kaganov, A. Pantsulaya, and A. Varlamov, Phys. Rep. **245**, 159 (1994).
[14] R. Hlubina, Phys. Rev. B **53**, 11344 (1996).
[15] R. Markiewicz, J. Phys. Chem. Solids **58**, 1179 (1997).
[16] J. M. Buhmann, Unconventional transport properties of correlated two-dimensional Fermi liquids, Ph.D. thesis, ETH Zurich, 2013.
[17] J. M. Ziman, *Principles of the Theory of Solids*, 2nd ed. (Cambridge University Press, Cambridge, U.K., 1972).
[18] J. M. Buhmann, M. Ossadnik, T. M. Rice, and M. Sigrist, Phys. Rev. B **87**, 035129 (2013).
[19] Y.-T. Hsu, W. Cho, A. F. Rebola, B. Burganov, C. Adamo, K. M. Shen, D. G. Schlom, C. J. Fennie, and E.-A. Kim, Phys. Rev. B **94**, 045118 (2016).
[20] K. Kadowaki and S. B. Woods, Solid State Commun. **58**, 507 (1986).
[21] A. C. Jacko, J. O. Fjærestad, and B. J. Powell, Nat. Phys. **5**, 422 (2009).
[22] J. M. Buhmann and M. Sigrist, Phys. Rev. B **88**, 115128 (2013).